ELSEVIER

Morphology-controlled nonaqueous synthesis of anisotropic lanthanum hydroxide nanoparticles

Igor Djerdj[a,d], Georg Garnweitner[b], Dang Sheng Su[c], Markus Niederberger[a,*]

[a]*ETH Zürich, Department of Materials, Wolfgang-Pauli-Strasse 10, 8093 Zürich, Switzerland*
[b]*Max Planck Institute of Colloids and Interfaces, Research Campus Golm, D-14424 Potsdam, Germany*
[c]*Department of Inorganic Chemistry, Fritz-Haber-Institute of the Max-Planck-Society, Faradayweg 4-6, D-14195 Berlin, Germany*
[d]*Department of Physics, Faculty of Science, University of Zagreb, Bijenička 32, P.O. Box 331, 10002 Zagreb, Croatia*

Abstract

The preparation of lanthanum hydroxide and manganese oxide nanoparticles is presented, based on a nonaqueous sol–gel process involving the reaction of La(OiPr)$_3$ and KMnO$_4$ with organic solvents such as benzyl alcohol, 2-butanone and a 1:1 vol. mixture thereof. The lanthanum manganese oxide system is highly complex and surprising results with respect to product composition and morphology were obtained. In dependence of the reaction parameters, the La(OH)$_3$ nanoparticles undergo a shape transformation from short nanorods with an average aspect ratio of 2.1 to micron-sized nanofibers (average aspect ratio is more than 59.5). Although not directly involved, KMnO$_4$ plays a crucial role in determining the particle morphology of La(OH)$_3$. The reason lies in the fact that KMnO$_4$ is able to oxidize the benzyl alcohol to benzoic acid, which presumably induces the anisotropic particle growth in [0 0 1] direction upon preferential coordination to the $\pm(1 0 0)$, $\pm(0 1 0)$ and $\pm(-1 1 0)$ crystal facets. By adjusting the molar La(OiPr)$_3$-to-KMnO$_4$ ratio as well as by using the appropriate solvent mixture it is possible to tailor the morphology, phase purity and microstructure of the La(OH)$_3$ nanoparticles. Postsynthetic thermal treatment of the sample containing La(OH)$_3$ nanofibers and β-MnOOH nanoparticles at the temperature of 800 °C for 8 h yielded polyhedral LaMnO$_3$ and worm-like La$_2$O$_3$ nanoparticles as final products.
© 2007 Elsevier Inc. All rights reserved.

Keywords: Nonaqueous synthesis; Solvothermal synthesis; Lanthanum hydroxide nanofibers; Transmission electron microscopy

1. Introduction

Lanthanides have been applied in various fields due to their electronic configuration (4*f* electrons) and lanthanide-based materials have interesting magnetic, optical, electrical, and nuclear properties. They have been widely used in phosphors for fluorescent lighting [1,2], semiconductors [3,4], or time-resolved fluorescence labels for biological detection [5]. Lanthanum, the lightest element among the lanthanides, has been extensively examined as oxide, hydroxide, phosphate, or oxychloride for optical [6,7], solid electrolyte [8], catalytic [9–11], and sorbent properties [12]. Especially, lanthanum hydroxide La(OH)$_3$ has been used as an intermediate step in the synthesis of the oxides

or sulfides through dehydration or sulfuration, because that approach is straightforward [13]. Hydroxyl groups may also act as active sites for surface grafting through condensation reactions of organic or biological reagents [14]. Recently, research was focused on two main features of La(OH)$_3$, namely its catalytic and sorbent properties. Concerning catalysis, La(OH)$_3$ as well as La$_2$O$_3$ is used as support for metals such as rhodium and platinum that are active for different reactions [11]. The major objective in terms of catalysis is to improve the catalytic capability, which can be achieved by the enlargement of the catalyst surface area, or/and by doping with selected metals like Ba, Pb or Cu [13].

It has been reported that La$_2$O$_3$ and La(OH)$_3$ are very sensitive to atmospheric conditions. When they are exposed to ambient carbon dioxide under ordinary conditions of temperature and pressure, the process of carbonation

*Corresponding author. Fax: +41 44 632 1101.
E-mail address: markus.niederberger@mat.ethz.ch (M. Niederberger).

occurs, leading to the formation of surface carbonates or hydroxycarbonates [12,15]. If the reaction temperature is higher than 450 °C, chemisorption of CO_2 results in $La_2O_2CO_3$. The influence of carbonates and oxycarbonates on the catalytic performances has been discussed for the oxidative coupling of methane reaction [16].

Material properties can often be significantly improved by producing particles in the nanometric range with controlled shape and size. Moreover, designing systems with lower dimensionality like nanofibers, nanowires, nanobelts or nanorods is of great importance due to the possible novel properties induced by the reduced dimensionality. In such systems carrier motion is restricted in two directions implying that they exhibit significant electron-transport properties different from the bulk material [17]. In this context the synthesis of $La(OH)_3$ compounds with quasi-one-dimensional morphology is important. Literature on the synthesis of $La(OH)_3$ nanoparticles with different morphologies is however scarce. The formation of $La(OH)_3$ nanotubes [18], nanowires, nanosheets, nanorods [17] and nanobelts [19] has been reported. The synthesis of these nanostructures was based on the preparation of rare earth hydroxide colloidal precipitates and the subsequent hydrothermal treatment at a designated temperature. The particle morphology was tuned by changing experimental parameters, particularly pH value of the aqueous solution [17,18]. In addition to these template-free routes to $La(OH)_3$ nanostructures, the synthesis of stable $La(OH)_3$ nanoparticles in water by performing hydrolysis and condensation reactions of lanthanum cations in the presence of block copolymers was reported, too. The asymmetry degree of the copolymer influenced both the size and the shape of the particles [20].

All these solution routes were performed in water as solvent. To the best of our knowledge, crystalline $La(OH)_3$ nanoparticles and nanostructures have not yet been synthesized using a nonaqueous sol–gel route. In comparison to reactions in aqueous media, the synthesis of nanoparticles in organic solvents seems to provide better control over particle size, shape, crystallinity, and surface properties [21–24].

In this work, we present a nonaqueous sol–gel route to $La(OH)_3$ nanoparticles with a variety of particle morphologies ranging from nanorods to nanofibers. The solvothermal reaction between lanthanum(III) isopropoxide and either benzyl alcohol, 2–butanone or a mixture thereof in the presence of $KMnO_4$ resulted in the formation of lanthanum hydroxide nanoparticles as main phase. The morphology, phase purity and crystallinity of the final products are controlled by simple variation of the $KMnO_4$ concentration without the use of any additional ligands or templates. Thermal treatment of the sample containing $La(OH)_3$ nanofibers and β-MnOOH nanoparticles resulted in the formation of polyhedral $LaMnO_3$ and worm-like La_2O_3 nanoparticles as final products. All the samples were investigated by powder X-ray diffraction (XRD), scanning electron microscopy (SEM), transmission electron micro-

scopy (TEM), combined high-resolution transmission electron microscopy (HRTEM), selected area electron diffraction (SAED) and energy-dispersive X-ray (EDX) analysis. Fourier transform infrared spectroscopy (FTIR) was used to investigate the organic and inorganic impurities attached to $La(OH)_3$ as well as to evidence the presence of OH groups. Analysis of the organic species in the final reaction mixture by ^{1}H and ^{13}C nuclear magnetic resonance (NMR) was performed in order to elucidate possible reaction mechanisms. We propose a model for the anisotropic growth of the $La(OH)_3$ nanoparticles taking the role of the solvents as well as of $KMnO_4$ into account.

2. Experimental Details

2.1. Materials

Lanthanum(III) isopropoxide (99.99 + %), potassium permanganate (99.99 + %), anhydrous benzyl alcohol (99.8%), and 2–butanone (99.5 + HPLC grade) were obtained from Aldrich and used as-received. The solvothermal treatment was performed in Parr acid digestion bombs with 45 ml Teflon cups.

2.2. Synthesis

All synthesis procedures were carried out in a glovebox (O_2 and $H_2O < 0.1$ ppm). The synthesis procedure was as follows: A mixture of 158.1 mg of La(OiPr)₃ (0.5 mmol) and 79.0 mg of $KMnO_4$ (0.5 mmol) was added to 20 mL of the organic solvents [benzyl alcohol, 2–butanone or a 1:1 vol. mixture thereof (10 mL benzyl alcohol and 10 mL 2–butanone]. In the case of the solvent mixture, the molar concentration of $KMnO_4$ was varied from 0.5, 0.25, 0.125 to 0 mmol, keeping the molar concentration of La(OiPr)₃ constant at 0.5 mmol. The reaction mixture was transferred into a Teflon cup of 45 mL inner volume, slid into a steel autoclave, and carefully sealed. The autoclave was taken out of the glovebox and heated in a furnace at 200 °C for 3 days. The resulting brown suspensions were centrifuged in order to separate the precipitate from the mother liquid. Excess organic impurities were removed by repeated washing steps in 10 mL of high-grade purity ethanol and chloroform and subsequently dried in air at 60 °C. Calcination of selected samples was performed at 800 °C for 8 h in air.

2.3. Characterization

X-ray powder diffraction (XRD) patterns were measured in reflection mode with CuKα radiation on a Bruker D8 diffractometer equipped with a scintillation counter. The instrumental contribution to the peak broadening caused by instrumental aberrations was removed by the deconvolution method with highly crystalline α-Al_2O_3 as a standard. Scanning electron microscopy (SEM) characterization including energy-dispersive X-ray (EDX)

microanalysis was performed with JEOL-JEM-6330F microscope operating at 15 kV. Transmission electron microscopy (TEM) measurement was performed on a Zeiss EM 912 Ω instrument at an acceleration voltage of 120 kV, while high-resolution transmission electron microscopy (HRTEM) characterization was done using a Philips CM200-FEG microscope (200 kV, $Cs = 1.35$ mm) equipped with a field emission gun. The samples for TEM characterization in a plane-view were prepared in a way that one drop of the dispersion of as-synthesized powder in ethanol was deposited onto a copper grid covered by an amorphous carbon film. To prevent agglomeration of nanoparticles the copper grid was placed on a filter paper at the bottom of a Petri dish. For cross-sectional TEM the samples were prepared using the ultramicrotomy procedure. The powder was added to gelatine capsule and subsequently filled with LRWhite resin. The capsules were dried for three days at 60 °C to allow polymerization. Afterwards, the capsules were trimmed to form the trapezoid. Ultrathin sections of approximately 50 nm thicknesses were cut using the ultramicrotome (UCT Leica) and mounted on copper grids. Fourier transform infrared (FTIR) investigations were performed on a Perkin-Elmer 2000 FTIR spectrometer. The formation mechanism for the metal hydroxide nanostructures was elucidated by characterization of the organic byproducts. The final reaction mixture was subjected to NMR and gas chromatography analyses after removal of the inorganic product by centrifugation. ^{1}H-BB-decoupled ^{13}C NMR measurements were performed on a Bruker DPX 400 spectrometer at 100 MHz, at a sample spinning rate of 20 Hz and with a ZG30 pulse program.

The structural and microstructural parameters were extracted using Rietveld refinement [25] with the program Fullprof [26]. The scale factor, the background coefficients, the zero point of the detector and the unit-cell parameters were simultaneously refined, followed by the refinement of the Gaussian half-width parameters, U, V, W, and the Lorentzian half-width parameters, X, Y. These parameters define the diffraction profile function, which was chosen to be the modified Thompson–Cox–Hastings pseudo-Voigt (T-C-H pV) [27], making the size analysis straightforward. In our approach we assumed that the line broadening of the deconvoluted profile was a result of the small crystallite size only, and therefore the values of half-width parameters U, V, W and X were kept constant at instrumental values determined by the α-Al$_2$O$_3$ standard. Due to the observed anisotropic size broadening, size analysis of such aniso-tropically broadened reflections was performed by fitting independently their size-like parameters. The background was taken to be the polynomial function of 2θ of the 5th order, because only in this case the best background modelling was obtained. The refinement incorporated weights w_i based on the observed step intensities Y_i, $w_i = 1/Y_i$. The refinement was continued until the shift in any parameter, Δx_i, was less than one third of its estimated standard deviation, σ_i. The quality of Rietveld refinement

was evaluated in terms of the discrepancy factor (profile-weighted residual error), R_{wp}, Bragg discrepancy factor R_B and the goodness-of-fit indicator, GoF.

3. Results and discussion

The lanthanum manganese oxide system was investigated by reacting La(OiPr)$_3$ and KMnO$_4$ with either benzyl alcohol (BA), 2–butanone (BUT), or a mixture of both solvents (BA + BUT) in the vol. ratio of 1:1. Furthermore, the influence of the KMnO$_4$ concentration on the particle morphology of La(OH)$_3$ was monitored in detail for the mixed BA + BUT system by variation of the molar ratios of La(OiPr)$_3$-to-KMnO$_4$ as follows: 1:1 [denoted as BA + BUT (1:1)], 1:0.5 [BA + BUT (1:0.5)], 1:0.25 [BA + BUT (1:0.25)], 1:0.125 [BA + BUT (1:0.125)] and 1:0 [BA + BUT (1:0)].

X-ray powder diffraction (XRD) patterns of the samples obtained are shown in Fig. 1. In all cases most reflections can be well indexed in the hexagonal La(OH)$_3$ structure with the space group $P6_3/m$ (ICDD PDF#36–1481). The corresponding Miller indices are denoted in the uppermost diffractogram for BA + BUT (1:1), i.e., the sample obtained in a mixture of BA + BUT with a La(OiPr)$_3$-to-KMnO$_4$ ratio of 1. One can clearly see that in addition to La(OH)$_3$ as major phase all samples, except the sample BA + BUT (1:0.5), contain crystalline byproducts.

The XRD pattern of the sample BA + BUT (1:1) shows additional reflections at 2θ positions of 19.23°, 33.75° and 37.95°, which can be assigned to β-MnOOH, mineralogical name Feitknechtite (ICDD PDF#18–804) [28]. According to the ICDD card this compound crystallizes in the tetragonal crystal system with the lattice constants $a = 8.6$ Å and $c = 9.3$ Å, however with unknown space
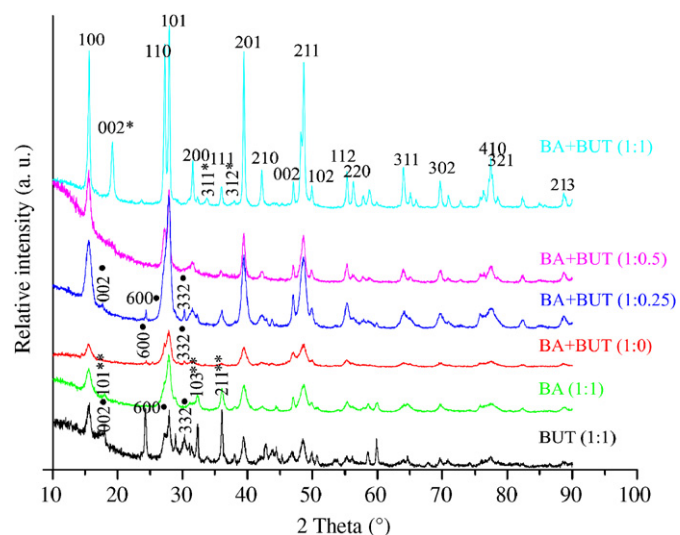
Fig. 1. XRD patterns of the samples in various solvents (BA, BUT and a mixture of BA + BUT) and La(OiPr)$_3$-to-KMnO$_4$ ratio (1:1, 1.0.5, 1:0.25 and 1:0). In addition to the Miller indices of the main La(OH)$_3$ phase, the three strongest reflections of identified minor phases are also denoted: *—β-MnOOH, **—Mn$_3$O$_4$ (Hausmannite), ●—LaCO$_3$OH.

group. The reaction in pure benzyl alcohol [BA (1:1)] yielded as minor phase Mn_3O_4-Hausmannite, tetragonal system, space group $I4_1/amd$ (ICDD PDF#24–734). The strongest well-resolved reflections of Mn_3O_4-Hausmannite are denoted in the XRD pattern with their Miller indices 1 0 1, 1 0 3, and 2 1 1. These results clearly prove the influence of the solvents on the product composition. While all other synthesis conditions are similar, the reaction in BA leads to Mn_3O_4-Hausmannite as minor phase, whereas in BA + BUT (1:1) β-MnOOH represents the byproduct. When the synthesis is performed in pure 2–butanone [BUT (1:1)] and in the mixture of benzyl alcohol and 2–butanone with molar La(OiPr)$_3$-to-KMnO$_4$ ratios of 1:0.25 [BA + BUT (1:0.25)] and 1:0 [BA + BUT (1:0)], the final products contain $LaCO_3OH$ as a minor phase. This compound crystallizes in the orthorhombic system with the space group $C222_1$ and with the unit-cell parameters $a = 21.891$ Å, $b = 12.639$ Å and $c = 10.047$ Å (ICDD PDF#29–744). The three strongest reflections of $LaCO_3OH$ are indexed 3 3 2, 6 0 0, and 0 0 2 in the respective powder patterns. A qualitative comparison of

the intensity of the strongest 6 0 0 reflections clearly shows that the fraction of $LaCO_3OH$ is the largest in BUT (1:1), significantly smaller in BA + BUT (1:0.25), and finally its presence in BA + BUT (1:0) is found only in traces.

The crystal structure was refined for La(OH)$_3$ and Mn_3O_4 only, while for the other compounds refinement was not possible due to the unknown space group (β-MnOOH), or missing fractional atomic coordinates ($LaCO_3OH$). The results of Rietveld refinement are summarized in Table 1, while the Rietveld refinement plot for the single-phase system BA + BUT (1:0.5) together with the difference curve is displayed in Fig. 2. Visual inspection of the difference curve confirms the good refinement and correct choice of the structural model. The quality of the fit is also estimated numerically in terms of weighted profile factor R_{wp} [29], whose values are given in the last row of Table 1. The best fit is achieved for the single-phase BA + BUT (1:0.5) XRD pattern, while for the other two-phase systems the R_{wp} values are higher. This is due to the presence of a second phase, which was not taken into account for refinement. Moreover, the increasing order of

Table 1
Structural data and refinement parameters for La(OH)$_3$ calculated by Rietveld refinement of XRD powder patterns.

|	BA + BUT (1:1)	BA + BUT (1:0.5)	BA + BUT (1:0.25)	BA + BUT (1:0)	BA (1:1)	BUT (1:1)
Phase 1	La(OH)$_3$	La(OH)$_3$	La(OH)$_3$	La(OH)$_3$	La(OH)$_3$	La(OH)$_3$
Space group	$P6_3/m$ (176)	$P6_3/m$ (176)	$P6_3/m$ (176)	$P6_3/m$ (176)	$P6_3/m$ (176)	$P6_3/m$ (176)
	$a = 6.532(1)$	$a = 6.528(1)$	$a = 6.517(1)$	$a = 6.524(2)$	$a = 6.515(2)$	$a = 6.534(2)$
Lattice parameters (Å)	$c = 3.855(4)$	$c = 3.853(3)$	$c = 3.853(3)$	$c = 3.857(1)$	$c = 3.854(1)$	$c = 3.856(1)$
	$\gamma = 120°$	$\gamma = 120°$	$\gamma = 120°$	$\gamma = 120°$	$\gamma = 120°$	$\gamma = 120°$
Cell volume (Å^3)	142.4(2)	142.2(2)	141.7(2)	142.2(1)	141.7(1)	142.6(1)
La site						
x	0.333	0.333	0.333	0.333	0.333	0.333
y	0.667	0.667	0.667	0.667	0.667	0.667
z	0.250	0.250	0.250	0.250	0.250	0.250
O site						
x	0.340(3)	0.340(3)	0.348(2)	0.346(4)	0.336(5)	0.36(1)
y	0.277(3)	0.289(3)	0.285(2)	0.284(4)	0.267(5)	0.30(1)
z	0.250	0.250	0.250	0.250	0.250	0.250
Isotropic average crystallite size (nm)	31.8	14.8	8.9	7.4	7.8	12.3
Special reflection broadening D_{002} (nm)	60.8	53.1	23.6	–	22.0	–
No. of reflections	52	52	52	52	52	52
Phase 2	β-MnOOH (Feitknechtite)	–	$LaCO_3OH$	$LaCO_3OH$	Mn_3O_4 (Hausmannite)	$LaCO_3OH$
Space group	unknown		$C222_1$ (20)	$C222_1$ (20)	$I4_1/amd$ (141)	$C222_1$ (20)
	$a = 8.6$		$a = 21.891$	$a = 21.891$	$a = 5.761(3)$	$a = 21.891$
	$c = 9.3$		$b = 12.639$	$b = 12.639$	$c = 9.446(5)$	$b = 12.639$
			$c = 10.047$	$c = 10.047$		$c = 10.047$
Lattice parameters (Å)						
	(ICDD PDF #18-804)		(ICDD PDF #29-744)	(ICDD PDF #29-744)		(ICDD PDF #29-744)
Cell volume (Å^3)	687.8		2779.8	2779.8	313.4(3)	2779.8
Average crystallite size (nm)					18.3	
No. of reflections					46	
No. of profile points	2668	2668	2668	2668	2668	2668
2θ step size (°)	0.03	0.03	0.03	0.03	0.03	0.03
R_{wp} (%)	22.9	12.4	16.1	18.3	17.8	29.0
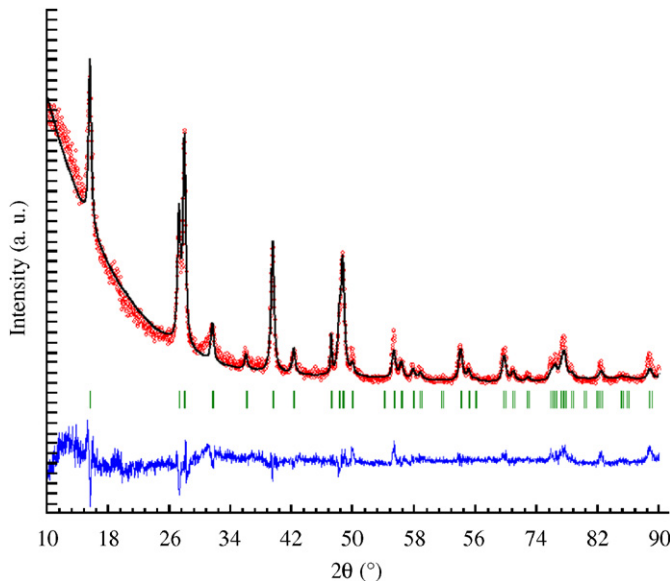
Fig. 2. Rietveld refinement plot for La(OH)$_3$ in the BA + BUT (1:0.5) sample. The observed intensity data (red) are plotted in the upper field. The calculated pattern (black) is shown in the same field as a solid-line curve. The difference curve (blue) is shown in the lower field. The short vertical bars in the middle field indicate the positions of the Bragg reflections of La(OH)$_3$.

Fig. 3. Full-width at half-maximum (FWHM) vs. 2θ for the reflections of La(OH)$_3$ synthesized in BA + BUT (1:0.5). With the exception of the 0 0 2 reflection, all other peaks follow a smooth functional curve.

R_{wp} for the systems containing LaCO$_3$OH is related to the increase of the LaCO$_3$OH fraction. In this way, the R_{wp} serves as a rough estimate for the quantity of the second phase. The calculated lattice parameters for the hexagonal La(OH)$_3$ structure are also given in Table 1. The values $a = 6.5286$ Å and $c = 3.8588$ Å fit well with ICDD data (ICDD PDF#36–1481). The slight variation of the calculated lattice parameter values with the synthesis conditions does not show any regularity or functional dependence on some measurable quantity such as crystallite size. Their small mutual differences can be regarded as simply originating from the refinement procedure. The calculated unit-cell volume values also agree well with each other. In addition to the unit-cell parameters calculation, the fractional atomic co-ordinates of La and O atoms are extracted, enabling a complete refinement of the La(OH)$_3$ structure. Due to the low electron density of the hydrogen atom, its fractional atomic co-ordinates cannot be determined from the XRD patterns.

For the Rietveld refinement, the sample synthesized in pure BA was considered as a two-phase system. Besides La(OH)$_3$, the Mn$_3$O$_4$-Hausmannite was also refined, and its calculated lattice parameters are $a = 5.761$ Å and $c = 9.446$ Å. Applying the procedure of Hill and Howard [30–32], the weight fractions (wt.%) of the two crystalline components were obtained and comprise 77.7 wt.% for La(OH)$_3$ and 22.3 wt.% for Mn$_3$O$_4$.

A qualitative analysis of reflection broadening in Fig. 1 already shows the influence of the isotropic crystallite size. However, a quantitative analysis of the reflection broadening in terms of full-width at half-maximum (FWHM)

points to the presence of anisotropic broadening (anisotropic crystallite size), which is in accordance with the morphology of the La(OH)$_3$ nanoparticles (see below). Fig. 3 displays the variation of the FWHM in dependence of the diffraction angle 2θ, extracted from the XRD pattern of the single-phase La(OH)$_3$ sample [BA + BUT (1:0.5)]. The plot indicates that the 0 0 2 reflection is considerably narrower (FWHM = 0.2°) than all the other peaks (FWHM in the range of 0.4–0.6°), pointing to an anisotropic shape of the crystallites with [0 0 1] as the preferred growth axis. Considering the nanofiber morphology (see TEM results below), this observation is consistent with the small crystallite size in two dimensions across the nanofiber and the larger crystallite size along the nanofiber axis. Similar findings have already been reported for CdTe nanowires [33]. Based on our FWHM analysis, we assumed that with the exception of 002 all the other reflections are equally broadened (isotropic case). Accordingly, reflection 002 was treated in FULLPROF subroutine as a special case. The whole broadening analysis was performed assuming that the line broadening of the deconvoluted profile occurs only due to the small crystallite effect, neglecting the presence of lattice microstrain. The results of the crystallite size calculation are also presented in Table 1. Comparing the isotropic crystallite sizes of the La(OH)$_3$ samples synthesized in a mixture of BA + BUT with different La(OiPr)$_3$-to-KMnO$_4$ ratios, one can notice that the average crystallite size decreases from 31.8 to 7.4 nm with decreasing the molar fraction of KMnO$_4$. The same trend occurs with the crystallite size measured along the [0 0 1] direction. In addition to the KMnO$_4$ concentration, also the solvent influences the final morphology of the La(OH)$_3$ nanoparticles, proven by a comparison of the isotropic crystallite sizes of the three samples obtained at a La(OiPr)$_3$-to-KMnO$_4$ ratio of 1 in different solvents [BA (1:1), BUT (1:1) and BA + BUT (1:1)]. In BA + BUT (1:1) the size is 31.8 nm, which is much larger than in the other two cases, where the isotropic crystal sizes do not differ much and are rather small (7.8 and 12.3 nm, respectively).

Representative TEM images of various La(OH)$_3$ nanoparticles are shown in Figs. 4(a)–(f) in dependence of the

synthesis conditions. In pure BA two types of nanoparticles located on separated areas on the TEM grid are observed. In addition to La(OH)$_3$ nanorods, small nanoparticles of Mn$_3$O$_4$ with irregular particle morphology are present, confirming the XRD results. The La(OH)$_3$ nanorods synthesized in pure BUT are considerably shorter (approximately 23 nm) in comparison with BA (about 47 nm), however with almost similar particle widths (8 and 10 nm, respectively). The average size in terms of particle length and width was estimated by measuring 100 particles in magnified TEM images. The results are summarized in Table 2.

Concerning the La(OH)$_3$ nanoparticles synthesized in a mixture of BA and BUT, it turned out that a change in anisotropy is observed in dependence of the KMnO$_4$ concentration. Decreasing the molar fraction of KMnO$_4$ results in a remarkable transformation of the particle morphology from highly anisotropic nanofibers several μm in length and with an average aspect ratio of more than 59.5 to nanorods just a few nanometers long (average aspect ratio of less than 10). Not only the length of the
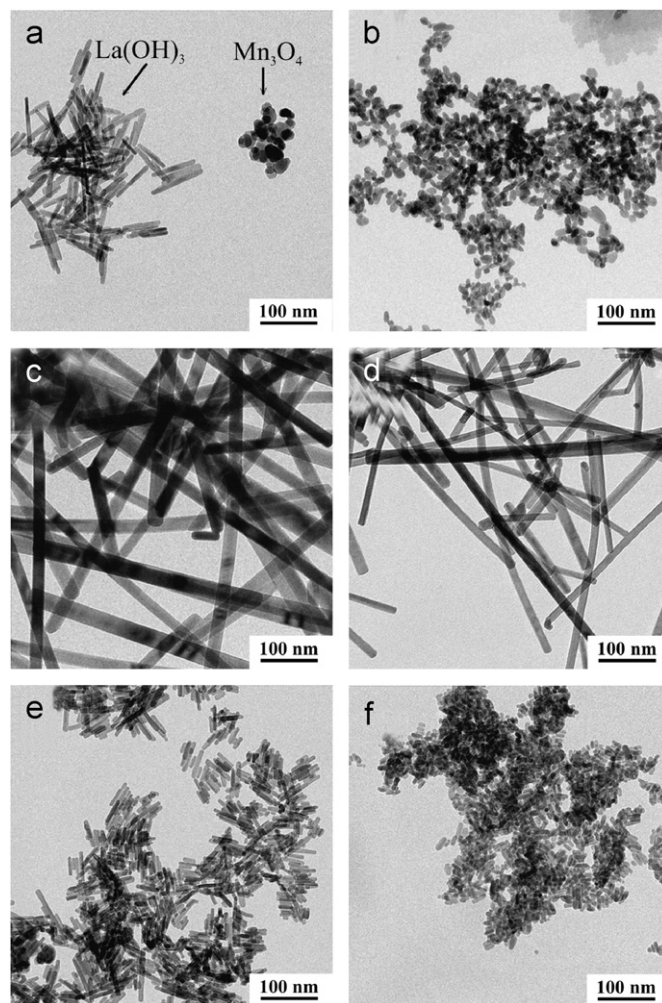
Table 2
Average dimensions (length, width) of La(OH)$_3$ nanostructures measured from TEM images.

	Average nanofiber/ nanorod length L (nm)	Average nanofiber/ nanorod width W (nm)	Average aspect ratio
BA (1:1)	47.2	8.5	5.5
BUT (1:1)	23.5	10.9	2.1
BA + BUT (1:1)	>1 μm	25.7	>38.9
BA + BUT (1:0.5)	>1 μm	16.8	>59.5
BA + BUT (1:0.25)	33.2	7.8	4.2
BA + BUT (1:0)	17.9	6.8	2.6

particles is altered, but also the width decreases from 25 nm in case of a La(OiPr)$_3$-to-KMnO$_4$ ratio of 1 to 7 nm for the sample without KMnO$_4$. These surprising results underline the importance of the concentration of KMnO$_4$ in determining the particle morphology in this nonaqueous synthesis process.

It is noteworthy that the lateral average dimension of the La(OH)$_3$ nanoparticles measured by TEM agrees well with the isotropic average crystallite size calculated from XRD. This implies that the isotropic broadening of the diffraction peaks relates to the crystallite size in the two dimensions across the nanofibers/nanorods. Figs. 5(a) and (c) show SEM images of the La(OH)$_3$ nanofibers synthesized in BA + BUT (1:1) and (1:0.5). For both synthetic conditions the nanofibers formed show high linearity. The nanofibers synthesized in BA + BUT (1:1) exhibit lengths up to 10 μm, which is considerably longer compared to the nanofibers obtained in BA + BUT (1:0.5), whose length is in the range of 1–2 μm. In accordance to TEM, the BA + BUT (1:0.5) nanofibers are narrower than the other sample, however with a much higher tendency to assemble into bundles and sphere-like agglomerates (see Fig. 5(c)). The corresponding EDX spectra of the La(OH)$_3$ nanofibers taken in the SEM mode are shown in Figs. 5(b) and (d). Besides the lines of the constitutive elements La and O, the EDX spectrum of the 1:1 sample has additional lines at 5.90 and 6.46 keV, which can be assigned to MnKα and MnKβ, giving further evidence for the presence of manganese in the form of crystalline β-MnOOH. In contrast to that, the EDX spectrum of the sample (1:0.5) gives no indication for manganese, confirming the phase-purity of the sample.

The thickness of the nanofibers seems to be rather small as judged from the HRTEM contrast (see below), exhibiting a morphology similar to that of nanobelts. For samples whose thickness measured parallel to the electron beam does not exceed 15 nm it is still possible to obtain lattice fringes in HRTEM [34]. Such consideration implies that the thickness of the La(OH)$_3$ nanofibers for which lattice imaging is possible (see below), is less or approximately equal to 15 nm. Further insight into the size and shape of the cross-section of the nanofibers was achieved using cross-sectional TEM. Fig. 6 shows a TEM image recorded in cross-section mode perpendicular to the


Fig. 4. Representative TEM images of the nanoparticles synthesized under various conditions. (a) BA (1:1), (b) BUT (1:1), (c) BA + BUT (1:1), (d) BA + BUT (1:0.5), (e) BA + BUT (1:0.25), (f) BA + BUT (1:0).
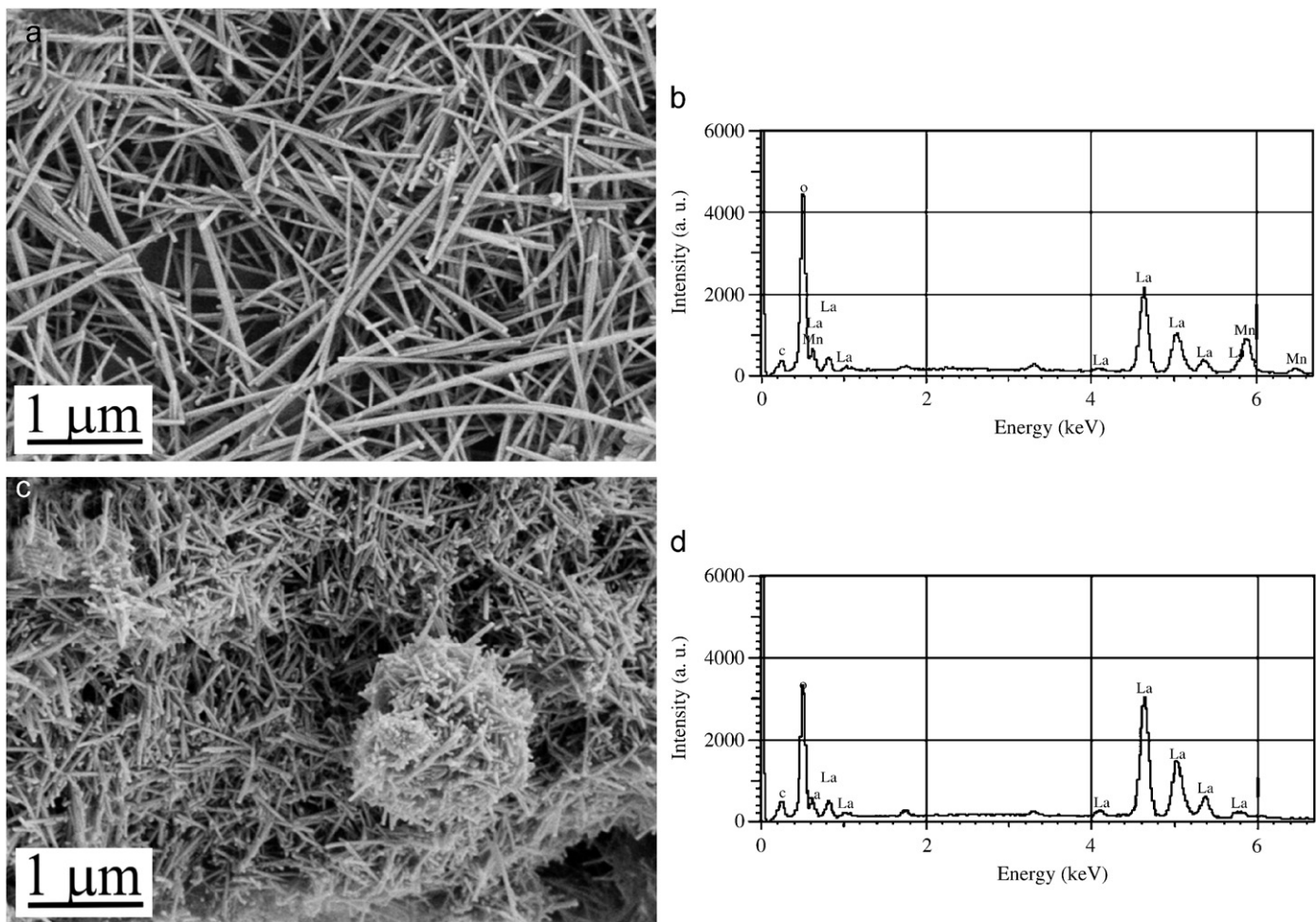
Fig. 5. (a) SEM image of the La(OH)$_3$ nanofibers in sample BA + BUT (1:1), (b) corresponding EDX spectrum, (c) SEM image of the La(OH)$_3$ nanofibers in sample BA + BUT (1:0.5), and (d) its EDX spectrum.
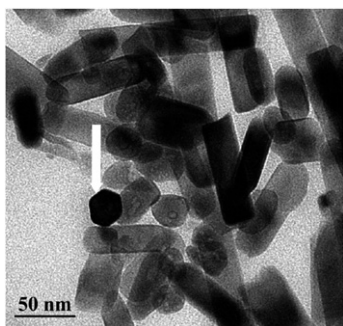

Fig. 6. Cross-sectional TEM image of La(OH)$_3$ nanofibers obtained in BA + BUT (1:1).

nanofiber axis for sample BA + BUT (1:1). According to this image, the cross-section of the nanofibers has mostly a rectangular shape with the shorter sides corresponding to the nanofiber thickness and ranging from about 18 to 30 nm. Obviously, the thickness is noticeable smaller than the width, which lies in the range of about 15–48 nm.

However, we have to point out that the long nanofibers observed in Fig. 6 are not all displayed in cross section, but rather along the tilted nanofiber axis. Due to the absence of parallel alignment of the nanofibers in 3D space uniform cross-sectional imaging is impossible. However, in some cases, the cross-section mode allows to observe well facetted shapes. Such a nanofiber nicely presented in cross section with a diameter of 29 nm is denoted with a white arrow in Fig. 6. It has a regular hexagonal shape with the top surface facet (0 0 1) and with the side surface facets along the fiber axis $\pm$(1 0 0), $\pm$(0 1 0), $\pm$(-110).

The structure of the individual nanofibers was further examined by HRTEM. Fig. 7(a) displays a HRTEM image of a part of a La(OH)$_3$ nanofiber in the sample BA + BUT (1:0.5) and imaged in the plane-view. The corresponding power spectrum, shown in the inset, is analyzed and indexed together with the SAED pattern in Fig. 7(b). The indexed spots match well with the XRD patterns of La(OH)$_3$ refined in the hexagonal system with the space group $P6_3/m$. The nanofiber is oriented along the [0 1 0] direction with respect to the electron beam, while its growth direction is along [0 0 1], i.e., along the c-axis. Such a growth direction, deduced from the analysis of the power spectrum, corroborates the results from cross-sectional
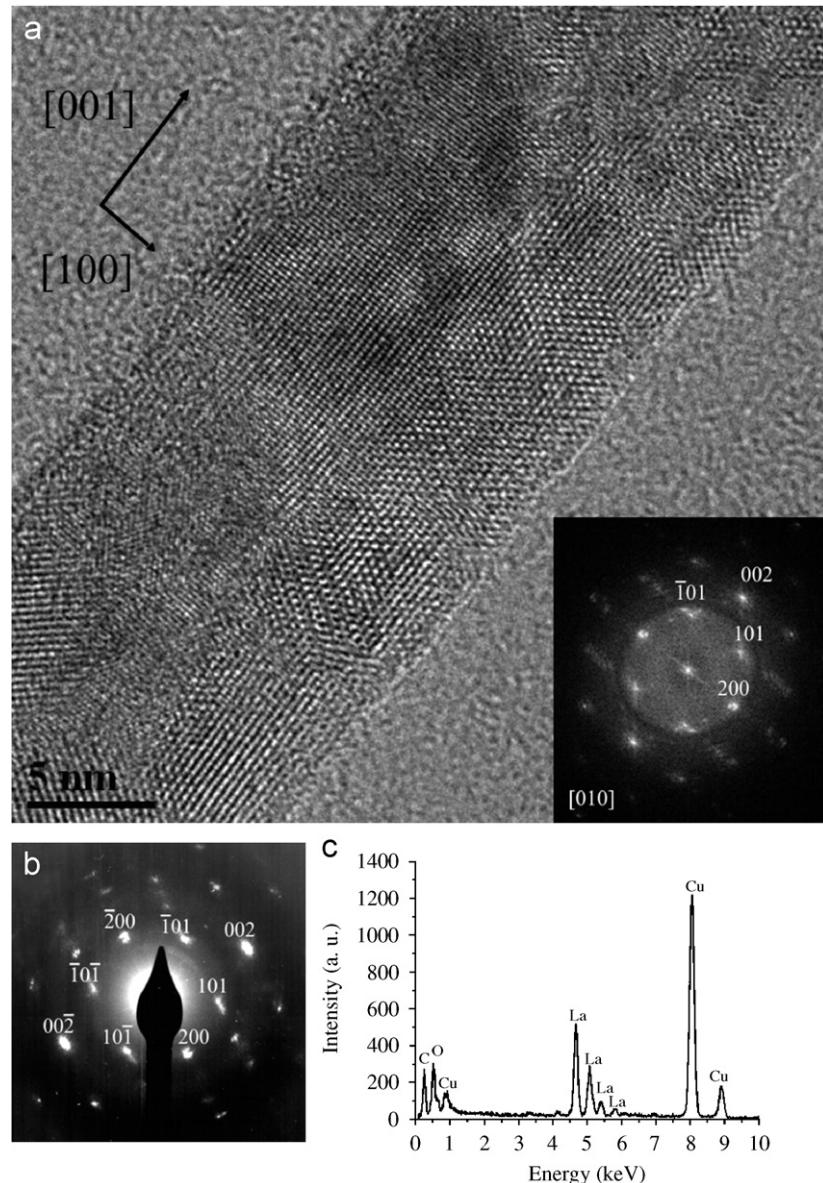
Fig. 7. (a) HRTEM image of a part of a La(OH)$_3$ nanofiber in the system BA + BUT (1:0.5) with its power spectrum as inset, (b) corresponding SAED pattern, (c) EDX spectrum.

TEM with the top surface represented by the well-facetted 0 0 1 surface as well as from the anisotropic broadening of the sharp 0 0 2 reflection in XRD. The HRTEM image also reveals that the surface of the nanofiber is not smooth, which manifests itself as a nonuniform focusing along the fiber axis. According to HRTEM and SAED, it seems that the nanofiber is composed of a single crystal. However, in hexagonal crystal systems and in particular in the case of a one-dimensional particle morphology (nanofibers, nanobelts, nanotubes, nanowires) there is a high probability that twins and stacking faults exist [35–37]. Indeed, in the lower part of Fig. 7(a) close to the nanofiber's edge, microtwins are clearly visible. Their presence here and in more general the presence of planar defects within nanofibers imply that nanofiber growth occurred from several nucleation centers

resulting in anisotropic defective structure similar as in the case of mesocrystals formation [38]. HRTEM images recorded from other areas of the sample also confirmed the presence of such defect features. By EDX microanalysis the constitutive elements La and O were detected. Similar to the results obtained in the SEM mode, no traces of Mn were found.

Fourier transform infrared spectroscopy (FT-IR) was employed as an additional probe to evidence the presence of OH groups as well as other organic and inorganic species. Fig. 8 displays the FT-IR spectra of the examined samples. An intense and sharp band at 3606 cm^{-1} and the band observed in the range of 623–636 cm^{-1} are characteristic of the stretching and bending OH vibrations of lanthanum hydroxide, respectively [12,15,39]. For all
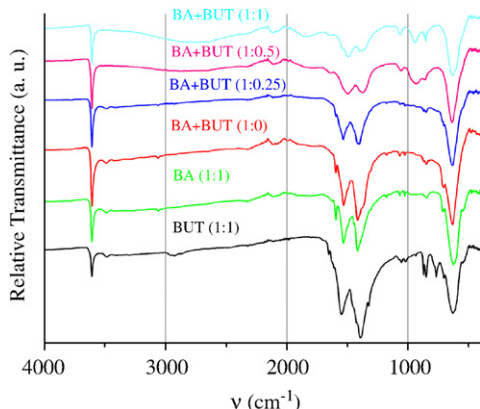
Fig. 8. FT-IR spectra of the samples in dependence of the solvents and La(OiPr)$_3$-to-KMnO$_4$ ratio.

samples excluding BA + BUT (1:1) and (1:0.5), the small and broad band around 3489 cm^{-1} is present, which can be assigned to H-bridge O–H vibration.

The most interesting range regarding the various surface adsorbed species is between 1200 and 1600 cm^{-1}. However, it is difficult to unambiguously assign all the bands present, because the carbonate peaks [15], the vibrations of aromatic rings [40] as well as O–C–O modes of benzoate [41] all appear within this area. In the samples BUT (1:1), BA (1:1), BA + BUT (1:0) and BA + BUT (1:0.25), the two intense bands are observed in the regions of 1373–1413 cm^{-1} and 1490–1548 cm^{-1}, corresponding to the ν_3 vibration of CO$_3^{2-}$ groups [15]. This is confirmed by two weak bands in the range of 1053–1061 cm^{-1} and 847–851 cm^{-1}, assignable to the ν_1 and ν_2 vibrations of CO$_3^{2-}$ groups, respectively. In the BA-BUT samples synthesized at higher KMnO$_4$ concentrations (1:0.5) and (1:1), the two bands appear at 1370 and 1500 cm^{-1}. Whereas the band at 1500 cm^{-1} can be assigned to the skeletal vibrations of the aromatic ring [40], the band at 1370 cm^{-1} may be due to O–C–O asymmetric and symmetric stretching modes of benzoate. However, the position of this band strongly varies in dependence of the metal oxide and the binding mode [42]. In addition, a small C = O stretching absorbance appears at 1648 cm^{-1}. According to the review paper of Bernal et al. [15], the rare earth sesquioxides as well as the hydroxides, when exposed to atmospheric CO$_2$ and H$_2$O at ordinary temperature, have a strong tendency to become hydrated and carbonated, which explains the carbonate bands in the IR spectra, also in cases, where no crystalline LaCO$_3$OH was detected by XRD.

The BA + BUT (1:1) sample was treated at 800 °C for 8 h in a postsynthetic step in order to investigate the further evolution of phase composition. According to Rietveld refinement of the XRD powder pattern (Fig. 9(a)), the final product contained only two phases, i.e., 43.7 wt.% of LaMnO$_3$ (s.g. $Pnma$, $a = 5.446(1)$ Å, $b = 7.742$ Å, $c = 5.503$ Å) and 56.3 wt.% of La$_2$O$_3$ (s.g. $P3m1$, $a = 3.9338(1)$ Å, $c = 6.1223(2)$ Å). The TEM image reveals two types of

particle morphologies (Fig. 9(b)). The nanoparticles with an anisotropic, worm-like shape can be assigned to La$_2$O$_3$ and originate from the La(OH)$_3$ nanofibers. The polyhedral nanoparticles represent LaMnO$_3$ and form upon the reaction of La(OH)$_3$ with β-MnOOH during calcination. Interestingly, no binary manganese oxide phases are found in this sample. The lattice fringes with a d-spacing of 2.77 Å in the HRTEM image of such a polyhedral nanoparticle can be assigned to the 1 2 1 reflection of LaMnO$_3$. This value does not overlap with any close equivalents of La$_2$O$_3$. Moreover, the EDX spectrum, taken from the region with polyhedral nanoparticles, shows the presence of strong manganese lines, whose intensity is comparable to the intensities of La and O lines (Fig. 9(d)) and additionally corroborates the identification of the polyhedral nanoparticles as LaMnO$_3$.

We have shown before that nonaqueous routes to metal oxides often proceed via complex and sophisticated organic reaction steps [24], involving such diverse processes as carbon–carbon bond formation [43] and cleavage [44], or aldol condensation [45]. Already in these rather simple systems, encompassing one solvent and one metal oxide precursor, some side mechanisms take place in addition to the main reaction, leading to a number of organic byproducts. For the systems discussed here, a mixture of solvents was used, as well as KMnO$_4$ with strongly oxidizing properties, leading to a plethora of species in the final solution. Therefore, we can just focus on some of the main routes. In both systems, no ethers were present in the final mixture, but large amounts of 2–butanol, indicating the occurrence of Meerwein–Ponndorf–Verley-like reduction–oxidation mechanisms, as we have described earlier (Fig. 10(a)) [43,45]. The concurrent oxidation of the isopropoxy ligands leads to acetone, coordinated in its enol tautomer, which induces aldol condensation with another ketone species (most probably, this would be 2–butanone as solvent as shown in Fig. 10(b)), simultaneously leading to the formal release of water in the course of the condensation reaction. In fact, especially in the BA + BUT (1:0.5) sample, containing smaller amounts of KMnO$_4$, significant quantities of higher α,β-unsaturated ketones, in particular 4–methyl-3–hexen-2–one, were found, confirming the assumption that mainly aldol condensation processes are the driving force for hydroxide formation.

In the case of the samples with higher amounts of KMnO$_4$, however, additionally the presence of benzoate species like benzyl benzoate was detected. Based on these results we infer that benzyl alcohol is oxidized to benzoic acid by the permanganate, and then undergoes condensation to the ester under (formal) release of water, as illustrated in Fig. 10(c). This mechanism is clearly preferred compared to aldol condensation and leads to faster release of water and hence a more rapid growth of the nanoparticles, also in form of hydroxides. The acicular shape of the lanthanum hydroxide nanocrystals can be explained by complexation of benzoate species selectively
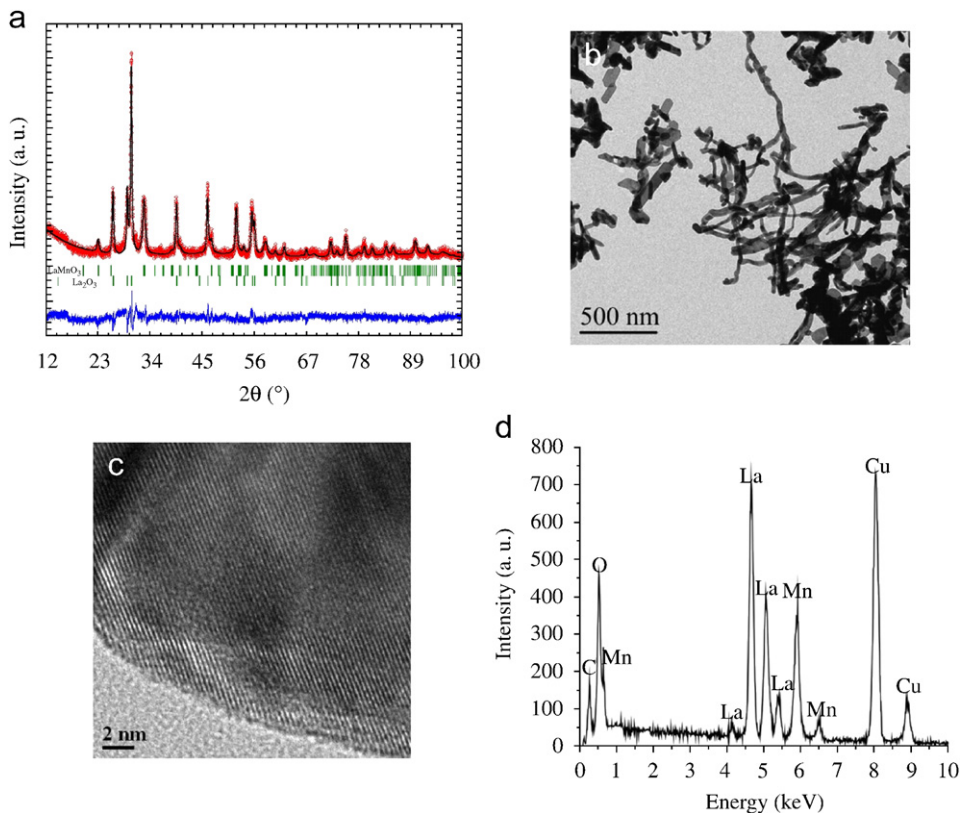
Fig. 9. (a) Rietveld refinement plot for the BA + BUT (1:1) sample calcined at 800 °C for 8 h, (b) TEM image of the same sample, (c) HRTEM image of a part of a polyhedral nanoparticle, (d) EDX spectrum taken from the region with excess of polyhedral nanoparticles.
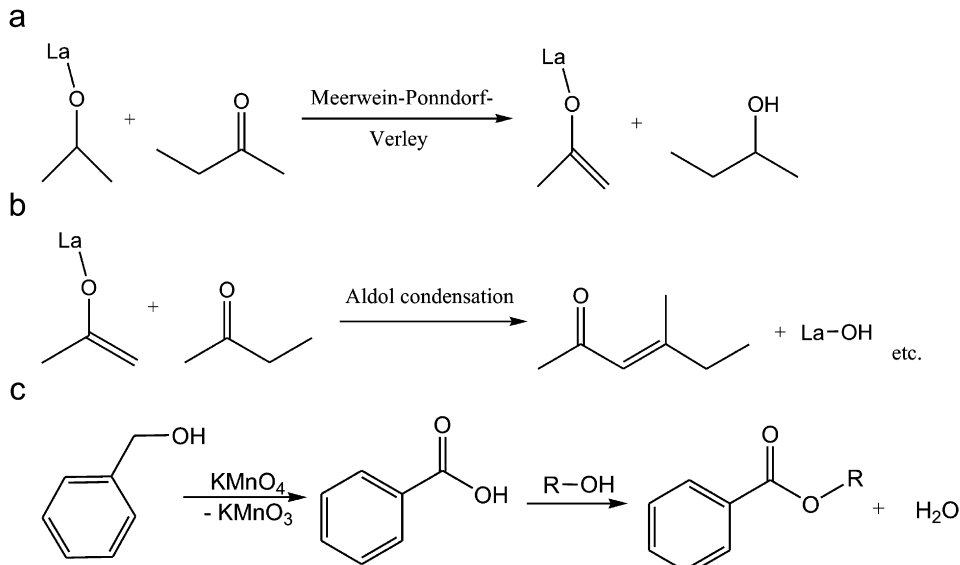

Fig. 10. Proposed reaction pathways involving (a) Meerwein–Ponndorf–Verley-like reduction–oxidation; (b) aldol condensation leading to the formation of a metal hydroxide species, and (c) oxidation of benzyl alcohol to benzoic acid by permanganate, followed by ester condensation and release of water.

to specific faces of the lanthanum hydroxide crystal. We have to point out that the addition of benzoic acid to the initial reaction mixture does not result in the crystallization of anisotropic lanthanum hydroxide nanoparticles, presumably due to instant esterification of benzoic acid with benzyl alcohol. Obviously, benzoic acid has to be formed in situ and parallel to the growth of the inorganic nanocrystals to fulfill its role as shape-controlling

agent. The oxidation of benzyl alcohol to benzoate or benzaldehyde during nanoparticle growth often leads to the formation of particle morphologies with reduced dimensionality such as nanolayers [46] or nanowires [47]. However, it must be mentioned that the obtained reaction solutions possessed intricate composition, and thus also other mechanisms, such as decarboxylation leading e.g., to diphenylmethane, or reactions involving C–C bond formation steps, cannot be excluded at the present stage of investigation.

4. Conclusions

The nonaqueous sol–gel reaction between lanthanum(III) isopropoxide and potassium permanganate in benzyl alcohol, 2–butanone and their equivolume mixture leads to formation of lanthanum hydroxide as main phase. In dependence of the molar ratio of the inorganic precursors and of the solvent used, various morphologies of $La(OH)_3$ nanoparticles were formed. In a 1:1 vol. mixture of benzyl alcohol and 2–butanone and for a molar $La(OiPr)_3$-to-$KMnO_4$ ratio of 1:1 and 1:0.5, the $La(OH)_3$ produced exhibits the shape of long nanofibers, while further decreasing the $KMnO_4$ concentration results in shorter nanorods with smaller cross-sections, i.e., with decreasing amount of $KMnO_4$, also the anisotropy of the particle morphology decreases. This observation can be explained by the fact that the acicular shape of the $La(OH)_3$ nanocrystals is presumably induced by the complexation of benzoate species, formed upon oxidation of benzyl alcohol by permanganate, selectively to all crystal faces of $La(OH)_3$ except the $0\,0\,1$ facet. Phase-pure samples containing only $La(OH)_3$ nanofibers were obtained in the BA + BUT mixture at a $La(OiPr)_3$-to-$KMnO_4$ ratio of 1:0.5. In this case, the nanofibers are well-crystalline with the growth direction along $[0\,0\,1]$. Postsynthetic thermal treatment of the BA + BUT (1:1) sample at $800\,°C$ for $8\,h$ yielded $LaMnO_3$ and La_2O_3 nanoparticles without any other binary manganese oxide phases. The results after calcination are in good agreement with a recently published work by Vazquez-Vazquez and Lopez-Quintela, who presented a detailed study on the nonaqueous synthesis of doped and undoped lanthanum manganite nanoparticles, however with nearly spherical particle morphology [48].

Acknowledgment

References

[1] G.S. Yi, B.Q. Sun, F.Z. Yang, D.P. Chen, Y.X. Zhou, J. Cheng, Chem. Mater. 14 (2002) 2910.
[2] B.M. Tissue, Chem. Mater. 10 (1998) 2837.
[3] A.R. Strzelecki, P.A. Timinski, B.A. Helsel, P.A. Bianconi, J. Am. Chem. Soc. 114 (1992) 3159.
[4] J.N. Huiberts, R. Griessen, J.H. Rector, R.J. Wijnaarden, J.P. Dekker, D.G. de Groot, N.J. Koeman, Nature 380 (1996) 231.
[5] C. Platas-Iglesias, L.V. Elst, W.Z. Zhou, R.N. Muller, C. Geraldes, T. Maschmeyer, J.A. Peters, Chem. Eur. J. 8 (2002) 5121.
[6] P. Schuetz, F. Caruso, Chem. Mater. 14 (2002) 4509.
[7] H. Meyssamy, K. Riwotzki, A. Kornowski, S. Naused, M. Hasse, Adv. Mater. 11 (1999) 840.
[8] N. Imanaka, K. Okamoto, G.Y. Adachi, Angew. Chem. Int. Ed. 41 (2002) 3890.
[9] A. Slagtern, Y. Schuurman, C. Leclercq, X. Verykios, J. Catal. 172 (1997) 118.
[10] E. Ordonez-Regil, R. Drot, E. Simoni, J.J. Ehrhardt, Langmuir 18 (2002) 7977.
[11] S. Irusta, L.M. Cornaglia, E.A. Lombardo, Mater. Chem. Phys. 86 (2004) 440.
[12] T.L. Van, M. Che, J.M. Tatibouet, M. Kermarec, J. Catal. 142 (1993) 18.
[13] S. Daniele, L.G. Hubert-Pfalzgraf, J. Sol-Gel Sci. Technol. 35 (2005) 57.
[14] S. Daniele, L.G. Hubert-Pfalzgraf, J. Vaissermann, Polyhedron 22 (2003) 127.
[15] S. Bernal, F.J. Botana, R. Garcia, J.M. Rodriguez-Izquierdo, React. Solids 4 (1987) 23.
[16] J.H. Lunsford, Catal. Today 6 (1990) 235.
[17] X. Wang, Y. Li, Angew. Chem. Int. Ed. 41 (2002) 4790.
[18] X. Wang, X. Sun, D. Yu, B. Zou, Y. Li, Adv. Mater. 15 (2003) 1442.
[19] C. Hu, C. Liu, W. Dong, Y. Zhang, G. Bao, C. Lao, Z.L. Wang, Adv. Mater. 19 (2007) 470.
[20] F. Bouyer, N. Sanson, M. Destarac, C. Gerardin, New J. Chem. 30 (2006) 399.
[21] M. Niederberger, G. Garnweitner, N. Pinna, G. Neri, Prog. Solid State Chem. 33 (2005) 59.
[22] M. Niederberger, G. Garnweitner, J. Buha, J. Polleux, J. Ba, N. Pinna, J. Sol-Gel Sci. Technol. 40 (2006) 259.
[23] G. Garnweitner, M. Niederberger, J. Am. Ceram. Soc. 89 (2006) 1801.
[24] M. Niederberger, G. Garnweitner, Chem. Eur. J. 12 (2006) 7282.
[25] L.B. McCusker, R.B. Von Dreele, D.E. Cox, D. Louer, P. Scardi, J. Appl. Cryst. 32 (1999) 36.
[26] J. Rodriguez-Carvajal, FULLPROF-A program for Rietveld Refinement, Laboratorie Leon Brillouin, CEA-Saclay, France, 2000.
[27] P. Thompson, D.E. Cox, J.B. Hastings, J. Appl. Cryst. 20 (1987) 79.
[28] O. Bricker, Am. Mineral. 50 (1965) 1296.
[29] R.A. Young, The Rietveld Method, Oxford University Press, Oxford, 1993.
[30] R. Hill, C.J. Howard, J. Appl. Cryst. 20 (1987) 467.
[31] I. Djerdj, A.M. Tonejc, J. Alloys. Compd. 413 (2006) 159.
[32] A. Gajović, I. Djerdj, K. Furić, D. Su, A. Tonejc, A.M. Tonejc, S. Musić, R. Schlögl, J. Am. Ceram. Soc. 89 (2006) 2196.
[33] S. Kumar, M. Ade, T. Nann, Chem. Eur. J. 11 (2005) 2220.
[34] B. Fultz, J.M. Howe, Transmission Electron Microscopy and Diffractometry of Materials, Springer, Heidelberg, 2001.
[35] X. Ma, H. Zhang, Y. Ji, J. Xu, D. Yang, Mater. Lett. 58 (2004) 1180.
[36] Z. Wang, L.L. Daemen, Y. Zhao, C.S. Zha, R.T. Downs, X. Wang, Z.L. Wang, R.J. Hemley, Nat. Mater. 4 (2005) 922.
[37] M.B. Salem, B. Yangui, G. Schiffmacher, C. Boulesteix, Phys. Status Solidi A 87 (1985) 527.
[38] H. Cölfen, M. Antonietti, Angew. Chem. Int. Ed. 44 (2005) 5576.
[39] G. Busca, V. Lorenzelli, Mater. Chem. 7 (1982) 89.

[40] M. Caravati, J.-D. Grunwaldt, A. Baiker, Phys. Chem. Chem. Phys. 7 (2005) 278.

[41] A. Tocchetto, A. Glisenti, Langmuir 16 (2000) 6173.

[42] C.A. Koutstaal, V. Ponec, Appl. Surf. Sci. 70/71 (1993) 206.

[43] M. Niederberger, G. Garnweitner, N. Pinna, M. Antonietti, J. Am. Chem. Soc. 126 (2004) 9120.

[44] N. Pinna, G. Garnweitner, M. Antonietti, M. Niederberger, J. Am. Chem. Soc. 127 (2005) 5608.

[45] G. Garnweitner, M. Antonietti, M. Niederberger, Chem. Commun. (2005) 397.

[46] N. Pinna, G. Garnweitner, P. Beato, M. Niederberger, M. Antonietti, Small 1 (2005) 112.

[47] J. Polleux, A. Gurlo, N. Barsan, U. Weimar, M. Antonietti, M. Niederberger, Angew. Chem. Int. Ed. 45 (2006) 261.

[48] C. Vazquez-Vazquez, M.A. Lopez-Quintela, J. Solid State Chem. 179 (2006) 3229.